Three-dimensional EM structure of the ectodomain of integrin αVβ3 in a complex with fibronectin

Brian D. Adair,[1] Jian-Ping Xiong,[3] Catherine Maddock,[4] Simon L. Goodman,[4] M. Amin Arnaout,[3] and Mark Yeager[1,2]

[1]Department of Cell Biology, The Scripps Research Institute, La Jolla, CA 92037
[2]Division of Cardiovascular Diseases, Scripps Clinic, La Jolla, CA 92037
[3]Structural Biology Program, Leukocyte Biology and Inflammation Program, Renal Unit, Massachusetts General Hospital and Harvard Medical School, Charlestown, MA 02129
[4]Oncology Research, Merck KGaA, Darmstadt 64271, Germany

Integrins are αβ heterodimeric cell surface receptors that mediate transmembrane signaling by binding extracellular and cytoplasmic ligands. The ectodomain of integrin αVβ3 crystallizes in a bent, genuflexed conformation considered to be inactive (unable to bind physiological ligands in solution) unless it is fully extended by activating stimuli. We generated a stable, soluble complex of the Mn^{2+}-bound αVβ3 ectodomain with a fragment of fibronectin (FN) containing type III domains 7 to 10 and the EDB domain (FN7-EDB-10). Transmission electron microscopy and single particle image analysis were used to determine the three-dimensional structure of this complex. Most αVβ3 particles, whether unliganded or FN-bound, displayed compact, triangular shapes. A difference map comparing ligand-free and FN-bound αVβ3 revealed density that could accommodate the RGD-containing FN10 in proximity to the ligand-binding site of β3, with FN9 just adjacent to the synergy site binding region of αV. We conclude that the ectodomain of αVβ3 manifests a bent conformation that is capable of stably binding a physiological ligand in solution.

Introduction

Integrins are αβ heterodimeric cell surface receptors that mediate cell–cell and cell–matrix interactions in metazoa (Hynes, 2002). Integrins are often expressed on the cell surface in an inactive state to prevent inappropriate cell–cell or cell–extracellular matrix adhesion (Arnaout, 2002). When cells are activated by a physiological stimulus, integrins rapidly and reversibly switch to an active (high-affinity) state as a result of intracellular signals that traverse the plasma membrane and alter the ligand-binding site; this is referred to as "inside-out" activation (for review see Hynes, 2002). Integrin activation can also be induced by the divalent cation Mn^{2+}, which binds to the ectodomain and mimics inside-out activation by its ability to activate the integrin in the absence of a bound ligand and to expose a similar profile of neoepitopes (for review see Hynes, 2002).

The X-ray crystal structure of the ectodomain of αVβ3 revealed a "head" attached to two "legs" (Xiong et al., 2001); in the native, full-length integrin, the legs connect to short transmembrane and cytoplasmic segments. The integrin head is formed by an NH_2-terminal, seven-bladed, β-propeller domain

of αV noncovalently bound to a vWFA-type domain (the βA domain) from β3. The αV leg is formed by an Ig-like "thigh" domain attached to two large colinear β-sandwich domains, designated calf-1 and calf-2 (forming the calf module). The β3 leg is formed by a PSI domain, an Ig-like hybrid domain, with βA projecting from one of its loops, four EGF-like domains, and a membrane proximal β-tail domain (βTD), which has a unique fold. In the crystal structure of αVβ3 in a complex with a pentapeptide containing the integrin-binding motif Arg-Gly-Asp (RGD), RGD bound at a crevice in the head between the β-propeller and βA domains, making extensive contacts with both (Xiong et al., 2002). An unexpected feature of the structure, also suggested by electron microscopy (Takagi et al., 2002), was that the legs were bent at the knees and folded back against the head (Xiong et al., 2001). The bend occurred between the thigh and calf-1 domains of αV and between EGF domains 1 and 2 of β3. Transmission EM of detergent-solubilized and rotary-shadowed (Nermut et al., 1988) or negatively stained (Takagi et al., 2002) integrins displayed extended molecules that would position the RGD-binding site ~200 Å from the plasma membrane (assuming that the calf module is perpendicular to the lipid bilayer). The presence of both bent and extended conformations suggested a "switchblade" (or jack-knife) model for affinity switching, whereby inside-out–driven leg separation straightens the integrin at the knees, converting the head to

Correspondence to M.A. Arnaout: arnaout@receptor.mgh.harvard.edu; or M. Yeager: yeager@scripps.edu

Abbreviations used in this paper: 3D, three-dimensional; βTD, β-tail domain; FN, fibronectin; FSC, Fourier shell correlation; RFC, reference-free classification.

the high affinity state (Beglova et al., 2002). However, other studies (Calzada et al., 2002; Butta et al., 2003) have suggested that genu straightening is not required to render the integrin competent to bind physiological ligands, and an alternative "deadbolt" model has been proposed (Xiong et al., 2003). Noting that the largest structural change between the liganded and unliganded crystal structures of the full-length αVβ3 ectodomain occurs in the F/α7 loop of βA, this model proposes that the CD loop from the βTD domain reaches into the βA domain of the native bent integrin and holds the F/α7 loop in a nonligand-binding form. Inside-out activation is then accomplished by releasing this deadbolt allosterically, $\sim$40 Å from the membrane, via cytoplasmic/intramembranous protein movements. Ligand binding then provides the energy for further conformational change, including perhaps genuextension, thus triggering outside-in signaling. This model assumes that the bent heterodimer can stably bind physiological, monomeric ligands in solution, the marker of the active state (Chigaev et al., 2001). To better understand the nature of the ligand-competent (active) form of an integrin, we performed EM studies of the ectodomain of αVβ3 in a stable complex with the physiological ligand fibronectin (FN).

Results

αVβ3 ectodomain forms a stable complex with FN7-EDB-10 in solution

Purified FN7-EDB-10 formed a stable complex with the αVβ3 ectodomain in solution at 37°C in the presence of 0.2–1.0-mM concentrations of the activating metal ion Mn^{2+} (Fig. 1); a complex with a fast off rate would have dissociated on the column (Takagi et al., 2003). Repeat chromatography showed that the purified complex did not dissociate over at least 3 wk at 4°C (unpublished data). Varying the ionic strength of the buffer from 5 to 145 mM NaCl did not have a significant effect on formation of the complex. 5-min exposure to pH 4.5 and a salt concentration of acetate used for negative staining did not dissociate the preestablished complex. The Stokes' radius of the integrin (based on peak shifts after gel filtration chromatography) changed from 60 ± 2.2 Å (mean ± SD, n = 9) in the unliganded Mn^{2+}-bound (Fig. 1) or Mg^{2+}-bound (unpublished data) state to a single symmetrical peak at 73 ± 1.2 Å (mean ± SD, n = 7) in the complex.

Unliganded and FN7-EDB-10–bound αVβ3 are compact particles

EM of negatively stained αVβ3 and αVβ3/FN7-EDB-10 in 0.2 mM Mn^{2+} displayed dispersed, compact particles as well as some particle aggregates (Fig. 2 A). By eye, there was no characteristic particle shape before image processing, suggesting that the particles did not have a preferred orientation on the grid. Nevertheless, discrete particle views that resembled the bent conformation of the crystal structure could be identified (Fig. 2 B). These V-shaped particle images can be interpreted as a globular head bent to contact the legs. Although few particles could be so easily interpreted, most were compact and not overtly extended. Examples of representative
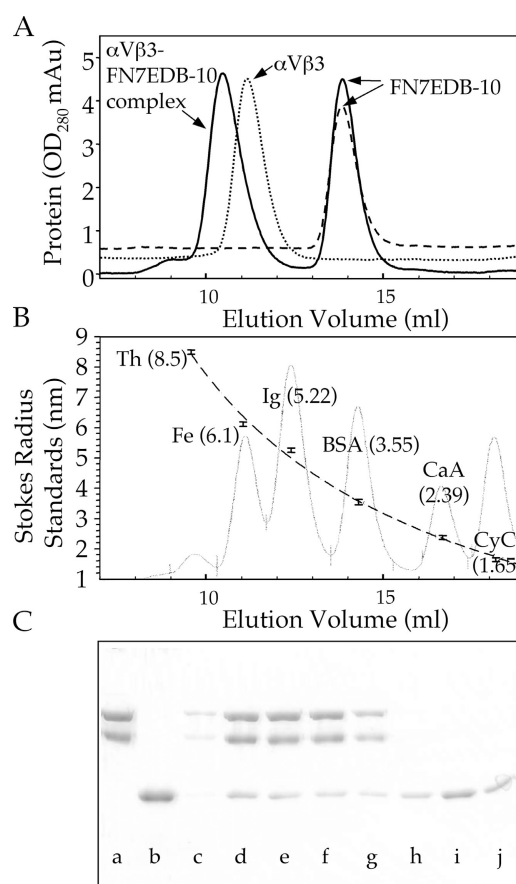

Figure 1. **αVβ3 ectodomain forms a soluble 1:1 complex with FN7-EDB-10 in solution.** (A) Salt-exchanged αVβ3 ectodomain (dotted curve), FN7-EDB-10 (dashed curve), or a mixture of the two (54 nmol of the integrin and 77 nmol of FN-7-EDB-10; solid curve) were resolved on a Superdex S-200 column in 1 mM Mn^{2+} buffer. When αVβ3 is mixed with excess FN7-EDB-10, the FN peak is retained, the unliganded αVβ3 is lost, and a new peak of the complex at a peak elution volume of 10.3 ml ($Rs \sim$7.3 nm) appears. (B) The elution profiles and the calculated Stokes' radii (Rs in nm) of the protein standards (indicated) and the fitted standard curve. The protein standards are Thyroglobin (Th), Ferritin (Fe), IgG (Ig), bovine serum albumin (BSA), carbonic anhydrase (CaA), and cytochrome c (CyC). Unliganded αVβ3 and FN7-EDB-10 elute as single symmetrical peaks at peak elution volumes of 11.3 and 13.8 ml, respectively. (C) Coomassie-stained 8% SDS-PAGE of the aliquots from eluted fractions (0.5 ml) of the stoichiometric mixture, showing the αV and β3 subunits of αVβ3 and FN7-EDB-10. Lane a, purified αVβ3 integrin; lane b, purified FN7-EDB-10. Lanes c–j column fractions: 9.5 ml (c), 10 ml (d), 10.5 ml (e), 11 ml (f), 11.5 ml (g), 13.5 ml (h), 14 ml (i), 14.5 ml (j). Note the approximate 1:1 stoichiometry of the chains in lanes c–g.

extended particles are displayed in Fig. 2 C; the first three images may show αVβ3 in a conformation where the leg calf-1/calf-2 module are colinear with the thigh domain of αV. A few particles also appeared to be bent at intermediate angles; e.g., the final three images in Fig. 2 C display an apparent $\sim$90° angle between the calf module and the thigh domain. As with the fully extended form, these intermediate forms were rare, in part because the angle is only clear in specific views of the particles. Only $\sim$5% of the hand-selected population of particles were clearly more extended than the bent αVβ3 crystal structure, but particle orientations on the grid appeared random (see below), so the actual percentage may
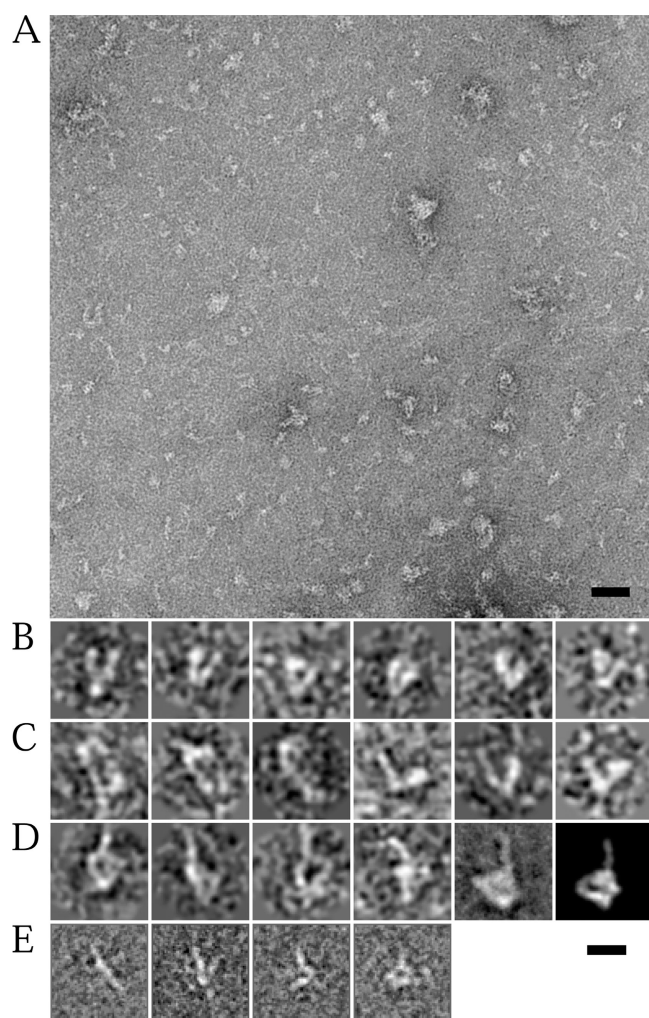
A

B

C

D

E

Figure 2. **Raw EM images of bent and extended forms.** (A) Field of integrin αVβ3/FN7-EDB-10 particles stained with uranyl acetate. The image has been subjected to a low-pass Fourier filter corresponding to the first node of the CTF. Bar, 500 Å. (B) A selection of raw αVβ3/FN7-EDB-10 particles that have a bent shape. For clarity, the particles have been subjected to a Fourier low-pass filter corresponding approximately to the first zero of the CTF. (C) A selection of raw αVβ3/FN7-EDB-10 particles that show a straighter, extended shape. The first three images show a fully extended form, whereas the last three images show an ∼90° bend. The particles have been filtered as in B. (D) Views of αVβ3 in a complex with FN7-EDB-10. The first four images are raw particles with a similar orientation to B, with additional density interpreted as FN7-EDB-10 projecting from the head. The fifth image is an average generated from a limited set of 304 manually selected raw particles specifically judged to be lying on their sides in the bent conformation with FN7-EDB-10 to be projecting from the head. The particles were subjected to reference-free alignment and classification. The average is from the largest of six groups, which contained 94 particles. The final image is a projection of a model of the αVβ3 X-ray structure in a complex with FN7-EDB-10. The image is the best match of the model with the average shown in the fifth image. (E) Averages of negatively stained FN7-EDB-10 from a manually selected data set of 352 particles and subjected to reference-free alignment and classification into 16 groups. The images, from left to right, are generated from 24, 25, 25, and 19 particles, respectively, and demonstrate a linear form on the left and forms with one or several bends between adjacent type III domains on the right (right three images). Bar, 100 Å.

be higher. For instance, extended forms viewed down the long axis would appear compact.
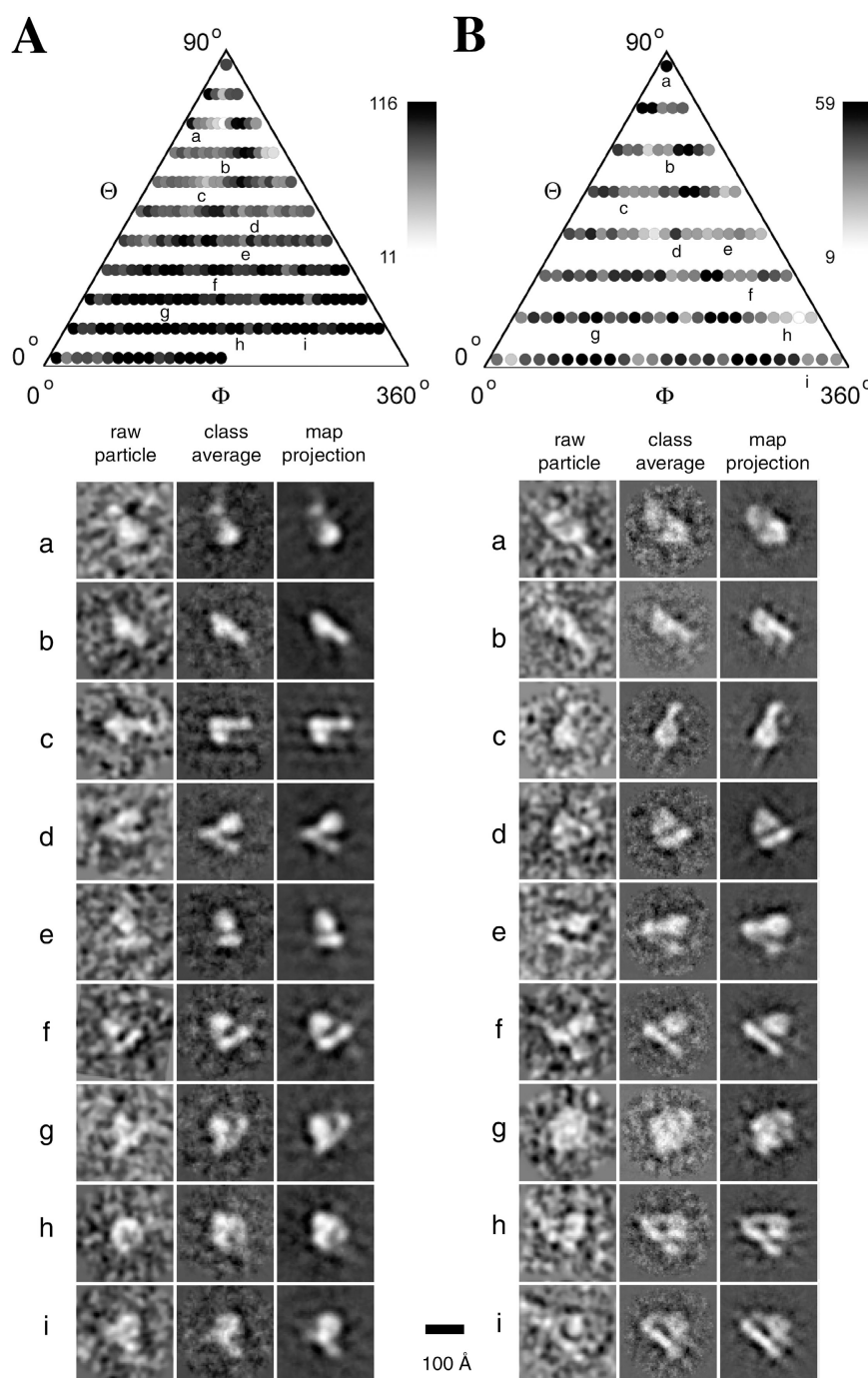
αVβ3/FN7-EDB-10 particles also appeared compact, as seen previously in rotary-shadowed EM images of α5β1

bound to FN (Gailit and Ruoslahti, 1988). In the majority of cases, it was not possible to distinguish αVβ3 domains from FN7-EDB-10. However, where we could identify individual integrin and FN domains in raw particles, the αVβ3/FN7-EDB-10 complex appeared to be bent (Fig. 2 D, first four raw images). This finding was verified by screening the negatives to specifically identify putative side-views of bent αVβ3. A total of 304 images were so selected and subjected to reference-free alignment and subsequent classification into six groups. An average of the group containing the largest number (94) of particles is displayed as the fifth image in Fig. 2 D. To compare this average with the bent form, a pseudoatomic model of αVβ3 with bound FN7-EDB-10 was generated and map projections calculated at 6° intervals. The sixth image in Fig. 2 D shows the projection that best matches the average. There is surprisingly good agreement between the two.

To determine if the majority of particles in the αVβ3/FN7-EDB-10 micrographs were genuinely in the bent conformation, an initial data set selected manually as for the unliganded sample was subjected to reference-free classification (RFC), where particle images were allocated into groups (∼50 particles each) followed by reference-free averaging of the resulting classes. Most averages resembled projections of the bent crystal structure of αVβ3. Only 3 of 23 classes (∼11% of the particles) were in a more extended form. To verify that most of the particles were not extended, an automatic particle selection routine using an extended integrin model (Xiong et al., 2001) was performed to bias the data set in favor of an extended conformation. None of these views resembled an extended integrin. We cannot exclude the possibility that unsampled regions on the grid might have preferentially arisen from aggregated extended forms. However, these are likely to be a minor species as the population applied to the grid was >95% monodisperse as judged by gel filtration chromatography (Fig. 1 A).

The compact, bent shape seen in projections from both the αVβ3 and αVβ3/FN7-EDB-10 samples resembled projections of the αVβ3 ectodomain in the presence of 1 mM Ca^{2+} (Takagi et al., 2002). However, in that work, the majority of particles in the presence of 1 mM Mn^{2+} or 1 mM Mn^{2+} plus RGD were in a fully extended conformation. This contrasts with our findings that a bent form predominated in 0.2 mM Mn^{2+}. To test for bias in our initial selection, an automated routine was used to select an additional 10,463 particle images from the αVβ3/FN7-EDB-10 micrographs based on a low-resolution envelope of a genuextended αVβ3 model (Xiong et al., 2001). RFC and alignment were performed in which images were divided into groups of ∼100 particles each, followed by reference-free averaging; no average resembled the extended, two-tailed forms shown in Fig. 2 of Takagi et al. (2002). Of the averages, 10 of 104 groups (858 particles) could be assigned to an elongated form with a single extended tail. It is also possible that features in the averages interpreted as the extended thigh and calf domains of αV were due to FN and that these images represent FN7-EDB-10 bound to a bent αVβ3. On the basis of the smaller hand-

Figure 3. Orientation distribution and projection views of uncomplexed αVβ3 and in a complex with FN. The top panels display histograms of the orientation distribution of raw images in each view of the final 18th round of refinement for free αVβ3 (A) and the 12th round of refinement for the complex between αVβ3 and FN7-EDB-10 (B). Images were aligned translationally (x and y) and rotationally in plane (ω), and each particle was assigned to the group to which it is best correlated (Adair and Yeager, 2002). Each circle represents a projection of the final model at a given (θ) and (φ) Euler angle (indicated on the axes). The intensity of each spot (black to white) is linearly proportional to the number of raw particles in that class reflected in the scale bar. The letters indicate spots (classes a–i) from which selected images with averaged views are shown. The left panels contain a raw particle image taken from the class (a–i). The middle panels contain the average calculated from all the particles in that class, and the right panels contain the map projection used to classify the particles. For clarity, the raw particles have been low-pass Fourier-filtered to approximately the first zero of the CTF.

selected data set, a larger set was selected using the same, automated model-based routine and a model of the αVβ3/FN7-EDB-10 complex. RFC and averaging of these 8,688 particle images yielded class averages that resembled the bent form of αVβ3. The majority of these averages did not display the rod-like extensions seen in the crystal structure of FN7-10 (Leahy et al., 1996), suggestive of bending between FN domains as seen in electron micrographs of full-length FN (Engel et al., 1981; Erickson and Carrell, 1983). This finding was verified by imaging the isolated FN7-EDB-10 fragment under the same buffer conditions as the complex. A total of 356 particle images were manually selected and subjected to RFC and

classification. Shown in Fig. 2 E are four of the classes, each based on averages of 19–25 raw particles. The left image (Fig. 2 C) shows a linear straight molecule, whereas the last three show multiple beads of density that we interpret as multiple bends between FN type III domains.

Random orientation of unliganded and liganded integrin particles on the carbon grid

The distribution of the refined orientation angles for the unliganded (Fig. 3 A) and liganded (Fig. 3 B) integrin samples showed that the particles adhered randomly to the carbon surface of the EM grids. The views covered the entire range of Euler an-
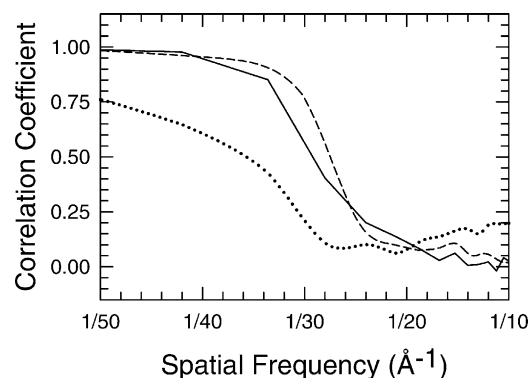
Figure 4. **FSC plot to estimate map resolution.** An FSC plot of the final round of refinement for free αVβ3 (solid curve) and in a complex with FN7-EDB-10 (dashed curve). Each data set was divided into two equal groups, the particles in each half data set were independently aligned with projections of the final model, and two independent maps were correlated in Fourier space. The solid and dashed curves cross the 50% threshold at ~30-Å resolution. The dotted line is the FSC between the final maps for the complex and uncomplexed samples (full data for each map). The two maps deviate from each other even at low resolution, indicating that the two structures are clearly different.

Figure 5. **EM integrin structures.** A refined surface-shaded density map of unliganded αVβ3 (A) and αVβ in a complex with FN7-EDB-10 (B). The maps were filtered to 30-Å resolution, and the isosurface contour level was set to the same 3.4 σ value for each map. The map in A is from the final (18th) refinement round and was generated using 8,841 particle images. The map in B is from the final (12th) refinement round and was generated using 3,722 particle images. (C) The difference map generated by superimposition of the αVβ3/FN7-EDB-10 complex map (B) on the αVβ3 map (A). The map (C) has been colored to indicate the residual density assigned to FN (yellow) and αVβ3 (green). In each panel, the middle view was generated by a z-axis rotation of the left view by 45 and 180° for the right view. Viewpoints in A–C are similar.

gles, so that all orientations were well represented. Selected raw images from each class with average views revealed that the integrin structure was fairly compact and resembled the bent shape of the X-ray structure (Fig. 3, A and B, image panels).

Three-dimensional (3D) maps of αVβ3 and αVβ3/FN7-EDB-10 complex display bent conformations

A 3D map of unliganded αVβ3 was reconstructed from an additional 10,542 images that were automatically selected from negatively stained samples. Orientations of the individual particles were determined by comparison with a reference set, iteratively generated from a 3D model. Particles outside the statistical cutoff criteria in the averages of equivalent views were rejected (~16% of the particles in the final round). The rejected particles may have represented αVβ3 in alternative conformations, particle aggregates, poorly stained particles, or denatured particles. The resolution of the map was estimated by Fourier shell correlation (FSC) analysis in which the data set was randomly divided in half, and two independently derived maps were compared in resolution shells in Fourier space. Using a conservative cutoff value of 0.5, the resolution was ~30 Å (Fig. 4, solid line). As suggested by particular views of the unprocessed particle images (Fig. 2 B) and class averages (Fig. 3), the compact 3D structure formed a roughly triangular wedge with sides measuring ~90 × 90 × 80 Å (Fig. 5 A).

A 3D map was also generated for the αVβ3/FN7-EDB-10 complex using 8,688 particle images that were automatically selected (Fig. 5 B). This map was generated from a dual model refinement in which one starting model was a low-resolution envelope of the αVβ3 crystal structure with the FN9-10 domains of FN, and the other was a low-resolution, rodlike envelope of FN7-EDB-10. This latter model was included because we were concerned that a flexed or bent population of free FN might be selected. The FN model (unpublished data)
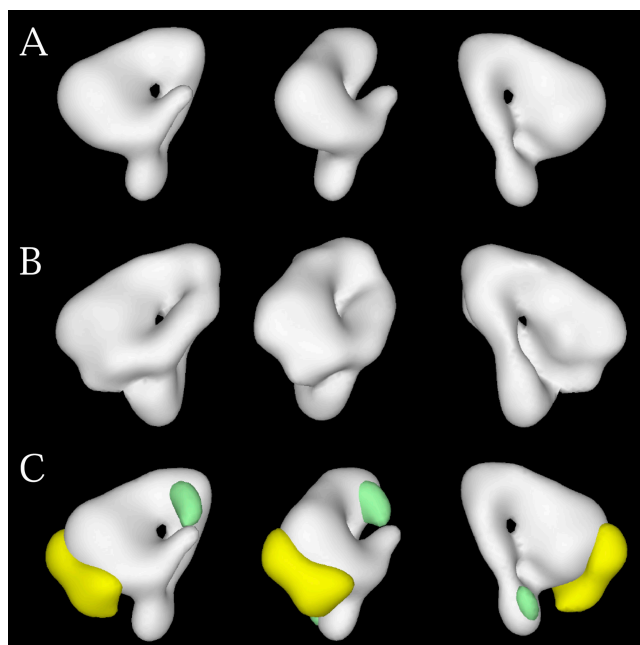
grew to resemble αVβ3 during the refinement, which allayed our concerns. The refined 3D map in Fig. 5 B was based on a final set of 3,722 particles, which displayed a random and well-sampled distribution of orientations (Fig. 3 B). The resolution of the map was comparable, if not slightly superior, to the uncomplexed map, as judged by FSC analysis (Fig. 4, dashed line). We also generated a map in which the refinement was based only on a model of the αVβ3/FN7-EDB-10 complex (unpublished data). In this case, more particles were included (~16% rejected by the alignment algorithm), and the map more closely resembled the ligand-free map.

Given the small size of the particles, the similar compact appearance even with bound ligand, and the difficulty in visualizing the bound FN7-EDB-10 in the unprocessed images, we also compared the 3D maps by FSC analysis. Although the two 3D maps in the absence and presence of FN7-EDB-10 did resemble one another, they were clearly not identical. FSC analysis showed ~75% correlation of the two maps at a resolution of 50 Å, which fell to <50% at ~35 Å resolution (Fig. 4, dotted line). This test demonstrated that the differences between the free and bound structures were even present in the low-resolution data where the signal to noise ratio was highest. To further test if the αVβ3/FN7-EDB-10 samples contained bent conformations of αVβ3, we tested two additional starting models: (1) a low-resolution envelope of an extended model of αVβ3/FN7-EDB-10 and (2) a
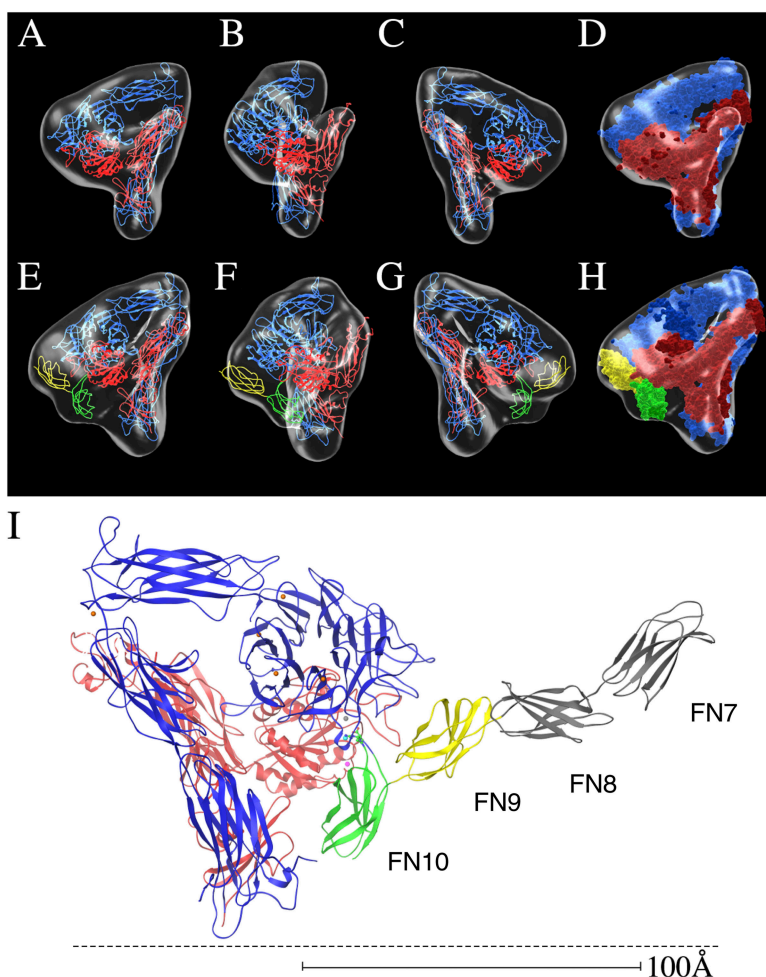
Figure 6. **Pseudoatomic models of unliganded and liganded αVβ3.** The red and blue chains are αV and β3, respectively. The FN9 (yellow) and FN10 (green) chains were derived from the X-ray structure of FN7-10 (Leahy et al., 1996) and were positioned such that the RGD loop of FN10 is superimposed on the cyclic RGD peptide in αVβ3 (Xiong et al., 2002). The isosurface levels for the maps have been set to 2.6 σ for each map. (A–C) A ribbon diagram of the αVβ3 crystal structure (Xiong et al., 2001) and the recently determined crystal structure of αVβ3 including the PSI domain (Xiong et al., 2004) fitted within the uncomplexed map. The views in B and C are produced by a rotation of the view in A by 135 and 180°, respectively. (D) The accessible surface of αVβ3 (1.4-Å probe radius) fitted in the map in the same view as C. The molecules in D are colored as in the ribbon models. (E–G) Ribbon diagrams of the αVβ3/FN9-10 complex fitted within the αVβ3/FN7-EDB-10 map in the same orientations as A–C. (H) An accessible surface model within the map viewed in the same orientation as G. (I) A ribbon diagram of a model of the X-ray structure of αVβ3 ectodomain in a complex with FN7-10 (Leahy et al., 1996) in the same orientation as in G. The FN10 RGD loop (positioned to superimpose on the cyclic RGD peptide in αVβ3) and the ligand Asp and Arg side chains are shown. αV and β3 are shown in blue and red, respectively. The ions at MIDAS (cyan), LIMBS (gray), and ADMIDAS (purple), the propeller base, and the αV genu (orange) are shown. The dotted line represents a putative position of the plasma membrane.

model generated by bootstrap methods using the reference-free alignment class averages, where a "common lines" algorithm was used to determine relative Euler angles for the averages. These refinements converged on a compact, triangular structure with dimensions comparable to the bent αVβ3 X-ray structure.

The EM grids were prepared from samples that had been maintained at 4°C. To determine if a similar structure existed at a physiological temperature, grids were prepared with material that had been incubated at 37°C for 1 h immediately before fixation on the grid. An initial data set of 4,461 particle images was selected from the αVβ3/FN7-EDB-10 complex by automatic methods using a model of the αVβ3 X-ray structure with FN. An initial reference-free alignment followed by classification into 89 groups showed a primarily compact structure (unpublished data). Only seven groups (∼8%), containing 218 particles, appeared to be more extended. The 3D analysis converged to a map that closely resembled the map generated from particles maintained at 4°C (Fig. 5 B). To evaluate bias in particle selection due to the reference model used, a data set of 4,191 particles was selected from the same micrographs using an extended model of αVβ3. The identical classification and averaging analysis were performed on this set. Of a total of 83 groups, 11 (∼13%), containing 471 particles, appeared to be in an extended conformation. On the basis of this analysis, we

concluded that the compact, bent form of the αVβ3/FN7-EDB-10 complex was also the predominant shape at 37°C.

Difference maps between unliganded and FN-liganded αVβ3

The map of αVβ3/FN7-EDB-10 has a shelf of density (Fig. 5 C, yellow) on the αVβ3 head in the difference map between the unliganded and FN-liganded structure. The starting model for the ligand-free map also included FN domains, yet the additional density was quickly lost in the refinement of images from samples with no bound FN. The density was present even if a single model was used in the refinement of the complex, and it also disappeared if two models were used to refine the uncomplexed αVβ3. The shelf of density can only accommodate two FN type III domains. We positioned the RGD motif of FN10 at the ligand-binding site in the pseudoatomic model, and FN9 was fit to the remainder of the density, thereby localizing the synergy site binding region in the β-propeller domain of αV. Density for the remaining domains (FN8, EDB, and FN7) was likely not visible because the FN7-10 fragment can adopt multiple conformations, with kinks between the domains (Erickson and Carrell, 1983; Litvinovich and Ingham, 1995; Takagi et al., 2003; Fig. 2 E), which would smear out the averaged density in the map of the complex.

As an additional test that the difference density was genuine, a further control was performed by randomly splitting the unliganded αVβ3 data set into two equal sets. 18 rounds of refinement were independently run for each of the sets. A difference map between the two unliganded maps did not display a shelf of density nor any density within the molecular volumes of the two maps (unpublished data). Differences were much smaller and randomly distributed throughout the reconstruction.

Comparison of the pseudoatomic model and the EM density envelope of αVβ3 showed additional density in the αVβ3/FN7-EDB-10 complex (Fig. 5 C, green) at the predicted location of the EGF1 and EGF2 domains of β3. These densities were poorly resolved in the X-ray structure and were not included in the starting model for the EM image analysis. There was also density attributable to the distal leg segments of αVβ3 (Fig. 5 C), with compensating negative density in the difference map on the opposite side of the stalk when the difference map was superimposed on the αVβ3/FN7-EDB-10 map. This density may be due to a movement of the stalk. Conformational changes in these regions in the FN-bound integrin may be sufficient to expose activation-sensitive or ligand-induced epitopes in the proximal and distal leg regions of the bent conformation. No separation of the legs in the FN-bound integrin ectodomain was observed at the ∼30-Å resolution of our maps.

There is a good fit of the crystal structures of unliganded and FN-liganded αVβ3 in the EM density envelope

The close resemblance between the low-resolution 3D EM map and the bent X-ray structure of αVβ3 enabled molecular docking (Fig. 6, A–D), with only a rotation of the hybrid domain by 11 ± 4° with respect to the X-ray structure. The hybrid domains were superimposable in the maps of free αVβ3 and the FN-bound complex, even when the X-ray structure was used as a starting model. The density corresponding to the hybrid domain extended from the end of the X-ray structure, as seen clearly in the map of the complex (Fig. 6, A, B, E, and F).

The extra shelf of density attributed to FN7-EDB-10 lies near the RGD-binding pocket in αVβ3 (Xiong et al., 2002). The RGD loop in FN resides in FN10, near the junction with FN9 (Leahy et al., 1996; Fig. 6 I). These constraints enabled us to place FN9 and FN10 within the density. FN10 was positioned so that the RGD loop was in proximity with the ligand-binding site at the interface between the αV β-propeller domains and the βA domain (Fig. 6 I). The remainder of the density accommodated FN9 so that it was just adjacent to the synergy site binding region on the αV β-propeller domain (Mould et al., 2003). Mutagenesis experiments showed that the α5β1 integrin bears a fairly extensive surface for the synergy site (Redick et al., 2000), and the contact area in our EM map suggests a similar interaction with αV. In the crystal structure of FN7-10, FN9 and FN10 are angled at ∼12° with respect to one another and bent away from the RGD loop. The fit of FN9 and FN10 into the EM density would improve if the bend were near 0°, bringing both domains flush with the αVβ3 head. Some flexion at the junction between FN9 and FN10 may be possible. In addition, the RGD loop is flexible in the X-ray (Dickinson et

al., 1994) and NMR structures of FN10 (Main et al., 1992; Copié et al., 1998).

Discussion

A completely unexpected and surprising feature of the X-ray crystal structure of the αVβ3 ectodomain was that the membrane proximal site was folded against the ligand-binding site in a bent, genuflexed conformation (Xiong et al., 2001). Because an extended conformation is thought to be required for ligand binding (Takagi et al., 2002), a second surprising result was that the bent conformation could bind a cyclic RGD peptide (Xiong et al., 2002). However, this result was achieved by soaking preformed crystals with a large excess of peptide. Although the folding of the 12 domains in the αVβ3 ectodomain was thought to be authentic, there have been concerns as to whether or not the bent conformation can stably bind physiological ligands in solution (i.e., exhibits the high affinity state). To examine this question, we used electron microscopy and image analysis to visualize the same αVβ3 ectodomain that was crystallized, as well as a complex with FN7-EDB-10. The main finding is that the bent form of the Mn^{2+}-bound, full-length αVβ3 ectodomain can bind FN7-EDB-10. Therefore, our work provides compelling evidence that the genuflexed conformation of the integrin ectodomain in solution is competent to form stable complexes with physiological ligands. A difference map comparing ligand-free and FN-bound αVβ3 revealed density that could accommodate the RGD-containing FN10 in proximity with the ligand-binding site and FN9 just adjacent to the synergy site binding region of αV (Fig. 6, E–H). One might expect that steric clashes would prevent binding of a large ligand such as FN to the bent conformation of the integrin ectodomain when attached to a membrane. However, the model in Fig. 6 I shows that it is indeed possible.

Binding of the αVβ3 ectodomain to FN7-EDB-10 is Mn^{2+} dependent and is reversed by Ca^{2+}, which is in agreement with the known roles of these divalent cations in integrin–ligand interactions (Humphries, 2000). The stability of the formed αVβ3/FN7-EDB-10 complex is consistent with (a) real-time measurements of integrin–ligand complexes, which showed that dissociation rate constants in physiologically activated cells are ∼10 times greater than for Mn^{2+}-treated cells (Chigaev et al., 2001) and (b) studies showing that dissociation of ligands from purified native integrins is slow compared with that in intact cells (Kouns et al., 1992; Cai et al., 1995).

An increase in the Stokes' radius from 56 (in 1 mM Ca^{2+}) to 60 Å induced by the activating cation Mn^{2+}, with a further increase to 63 Å upon addition of cyclic RGD, has been used as an independent indicator to substantiate genu straightening as a prerequisite for inside-out activation of integrins (Takagi et al., 2002). We have verified this shift in gel filtration profiles as well (yielding calculated Rs values in 1 mM Ca^{2+}, 1 mM Mn^{2+}, and 1 mM Mn^{2+}+cyclic RGD of 57 ± 2.5 [$n = 7$], 60 ± 2.2 [$n = 9$], and 64 ± 1.6 Å [$n = 4$], respectively). The calculation of Stokes' radius is derived from comparison of elution profiles of well-behaved monomeric proteins with known standards. However, the interpreta-

tion of the Stokes' radius in terms of molecular shape can be complicated by several factors. For example, transient dimers in rapid equilibrium can have a substantial effect on elution profiles of proteins in gel filtration chromatography (Winzor and Scheraga, 1963), and we know that the specimens do contain a small fraction of aggregates (Fig. 2 A). Perhaps relevant is the recent finding that Mn^{2+} but not Ca^{2+} can induce formation of dimers and higher order multimers of purified, full-length $\alpha IIb\beta3$ integrin (Litvinov et al., 2004). We have also observed reversible multimerization of the ectodomain by gel filtration chromatography in Mn^{2+} but not Ca^{2+} (unpublished data). In addition, the estimation of an axial ratio within a complex assumes that the complex is formed by rigid bodies. In our case, we know that the bound FN7-EDB-10 exhibits substantial conformational flexibility (Fig. 2 E). It is also noteworthy that solution X-ray scattering profiles will be influenced by particle aggregation and multiple conformational states. For these reasons, electron microscopy and single particle analysis provides an appealing method to study the structure of integrin complexes in solution, especially because objects of an inappropriate size (such as aggregates) can be excluded.

Only one other paper examined the EM structure of the full-length $\alpha V\beta3$ ectodomain in the presence of different cations and the absence of detergent (Takagi et al., 2002). These authors found that the vast majority ($\sim$85%) of the unliganded $\alpha V\beta3$ ectodomain becomes fully extended from a largely bent conformation when 1 mM Mn^{2+} replaces Ca^{2+}, which is in parallel with an observed shift in the protein gel elution profile (a change in calculated Rs from 57 to 60 Å). Addition of cyclic RGD increased the proportion of extended forms to $\sim$95%. Although we observed similar shifts in calculated Rs values, the bent conformation was the predominant shape with or without bound FN. We note that the images obtained from class averages of the integrin in Mn^{2+} in the previous paper (Takagi et al., 2002) were generated from a sample where more compact forms were excluded before processing. As a result, it is not possible to directly compare the compact form seen by Takagi et al. (2002) in Mn^{2+} with the compact form we observed. Takagi et al. (2002) also used manual selection of individual particle images and examined averages of two-dimensional projections. In contrast, we used an automated routine with no attempt to visually reject particles other than obvious aggregates, and we generated a 3D map by an iterative classification and averaging process. Projections from the 3D map provided a way of identifying and classifying all selected particles, and the use of multiple iterations ensured that the resemblance to the initial model was not due to alignment of noise (Grigorieff, 2000). Lastly, we examined the native ectodomain of $\alpha V\beta3$, whereas the previous paper examined a modified protein: a 13–amino acid sequence containing a tobacco etch virus (TEV) proteolytic cleavage site was inserted at the COOH-terminal end of the calf2 domain, followed by an acidic 30-residue stretch, and a cysteine residue was added at the COOH terminus of the βTD, followed by a basic 30–amino acid sequence, terminating with a histidinex6 tag. Heterodimer formation in this recombinant $\alpha V\beta3$ is mediated not only by the natural association of the βA and the αV β-propel-

ler domains but also by both an intersubunit disulfide bond and a long acidic–basic, coiled-coil segment. Such modifications may affect the shape of the Mn^{2+}- or Mn^{2+}+RGD-treated integrin after grid adsorption and fixation.

A recent EM study of a legless fragment of the $\alpha5\beta1$ ectodomain in complex with FN7-10 showed density for bound FN10 but not FN9 (Takagi et al., 2003). The FN-bound form exhibited a dramatic $\sim$80° opening of the angle between the hybrid and βA domains (Takagi et al., 2003). In the presence of a linear RGD peptide, this $\alpha5\beta1$ fragment had a range of hybrid angles, with $\sim$75% of the molecules showing the wider $\sim$80° angle. This outward swing of the hybrid domain was also seen in recent X-ray crystal structures of a similarly truncated form of $\alpha IIb\beta3$ in complexes with ligand mimetics or with a monoclonal antibody (Xiao et al., 2004). Low-angle X-ray solution scattering patterns of an extracellular fragment of the $\alpha5\beta1$ ectodomain with truncated legs and in complex with FN6-10 were consistent with a more limited 45° outward swing of the hybrid domain relative to βA in the FN-bound form (Mould et al., 2003). In the model, FN contacted the integrin through the synergy site in FN9 (Mould et al., 2003). Our EM maps suggested a much smaller outward swing of the hybrid domain, $\sim$10°, in both the unliganded and liganded states of $\alpha V\beta3$. The two previous studies used soluble ectodomain fragments missing the leg domains calf1, calf2, EGF1-4, and βTD; perhaps their absence allowed greater conformational flexibility of the hybrid domain. Additional differences between the two ectodomain fragments of $\alpha5\beta1$ may account for the binding of the synergy site to one integrin fragment (Mould et al., 2003) but not to the other (Takagi et al., 2003).

The major conclusion of this work is that the bent $\alpha V\beta3$ ectodomain stably binds a physiological ligand in solution in a Mn^{2+}-dependent manner. Although this study does not address the mechanisms by which the native membrane-bound integrin is activated by inside-out signals, Mn^{2+}-induced activation of the ectodomain, as reflected by stable binding to ligand in solution, suggests that this activation can take place through small local conformational changes (Xiong et al., 2003). This ability of the integrin to maintain stable ligand interaction in the bent state may be relevant during internalization, interaction of ligands with coreceptors, microfibril assembly, and extracellular matrix assembly and remodeling. Additional conformational changes of the membrane-bound integrin that include various degrees of genuextension may be ligand induced and a feature of outside-in signaling.

Materials and methods

Protein expression, complex formation, purification, and characterization
Preparation and properties of a recombinant ectodomain of human integrin $\alpha V\beta3$ have been described previously (Mehta et al., 1998). A cloned fragment of human FN consisting of five type III repeats, 7–10, plus the inserted EDB domain (between domains 7 and 8; designated FN7-EDB-10) was provided by I. Aukhil (University of North Carolina, Chapel Hill, NC; Leahy et al., 1996). An NH2-terminal (Met-Gly-Ser-Ser) spacer and a (His)6 tag facilitated purification by immobilized metal affinity chromatography. The complex was formed by mixing the $\alpha V\beta3$ ectodomain and FN7-EDB-10 in a 1:1.5 stoichiometric ratio in solution for 1.0–1.5 h at 37°C in 145 mM NaCl, 5 mM KCl, 25 mM Tris-HCl, pH 7.4, buffer (TBS) containing 1 mM $MgCl_2$, 1 mM $CaCl_2$, or 0.2 mM

MnCl$_2$. Unbound molecules were separated at RT from the complex by molecular sieve chromatography on a precalibrated Superdex S-200HR (10/30) column (0.9 × 30 cm; Amersham Biosciences). Fractions containing the complex were identified by SDS-PAGE, pooled, dialyzed, and stored at 4°C in TBS containing 0.2 mM MnCl$_2$. The Stokes' radii of αVβ3, FN, and the complex were derived by substituting their peak elution volumes (Ve) in the equation $Rs = (a + b*Ve)/(c + Ve)$, where the constants a, b, and c are 102.3647, −4.1089, and −2.1021, respectively. Identity of the resolved peaks was confirmed by SDS-PAGE and by ELISA using the mAb LM609 to αVβ3 (Cheresh and Spiro, 1987) and polyclonal anti-FN antibodies (BiosPacific). Formation of the αVβ3 complex was RGD mediated and Mn^{2+} dependent. The complex did not form in TBS containing 1 mM CaCl$_2$ alone. Exchanging CaCl$_2$ for MnCl$_2$ dissociated the preformed complex.

EM and image analysis

The free αVβ3 ectodomain and the complex with FN7-EDB-10, each at ~1 mg/ml in 2.5 mM Tris-HCl, pH 7.4, 15 mM NaCl, and 0.2 mM MnCl$_2$, were incubated for ~5 min at RT on carbon-coated grids rendered hydrophilic by glow discharge in the presence of amyl amine. The grids were blotted, washed twice in 0.05 mM MnCl$_2$, twice in 0.5% uranyl acetate, and incubated for 1 min in 0.5% uranyl acetate, pH 4.5. Uranyl acetate is a rapid protein fixative that can preserve even labile biological structures (Zhao and Craig, 2003). The grids were blotted and then air dried. EM was performed using a CM200 (for the complex; Philips Electron Optics/FEI) and CM120 (for free αVβ3; Philips Electron Optics/FEI), both operating at 100 kV. Images were recorded on film (SO163; Kodak) at a nominal magnification of 50,000 (CM200) or 45,000 (CM120). Micrographs were digitized on an SCAI scanner (Carl Zeiss MicroImaging, Inc.) at 8 bits and 7 μm^2/pixel. Digitized images were subjected to three-fold pixel averaging to generate final images at 4.20 (CM200) and 4.67 (CM120) Å/pixel. Images of free FN7-EDB-10 in solution were recorded at a magnification of 60,000 (CM120), and digitized micrographs were averaged to 3.5 Å/pixel.

Particle selection and 3D reconstruction were performed using the EMAN suite (Ludtke et al., 1999). Additional particle alignment and classification were performed with SPIDER (Frank et al., 1996). The contrast transfer function for each micrograph was determined, and phase corrections were applied to each particle. For manual particle selection, particle images were visually identified and selected on the basis of an appropriate size and separation from other particles. Particle images were initially aligned by a reference-free algorithm, and then classified using factor analysis and k-means grouping (Adair and Yeager, 2002). For automated particle selection, a set of reference projections was generated from an initial 3D model. 3D maps were generated by an iterative refinement method. Particles were classified by a real-space cross-correlation search with reference projections computed at 12 to 9° intervals. Particles in each projection class were averaged, and a 3D map was generated by Fourier back-projection methods. The resulting model was used for subsequent rounds of refinement. The iterations were halted when the FSC between the current and previous models did not show any significant difference. To ensure that the complex did not dissociate, some specimens were supplemented with free FN7-EDB-10. The processing of these images used two initial starting models, the bent conformation of αVβ3 and a highly bent model of free FN7-EDB-10, and projections were produced for both. Particles were classified by cross-correlation with the combined projection set, and each particle was assigned to a single class. After averaging the particles in each class, two new models were generated by separating the averages into the appropriate starting group and then calculating back projections. All surface-shaded representations were visualized using AVS software (Sheehan et al., 1996).

Note added in proof. A recent study (Wei, Y., R.P. Czekay, L. Robillard, M.C. Kugler, F. Zhang, K.K. Kim, J.P. Xiong, M.J. Humphries, and H.A. Chapman. 2005. *J. Cell Biol.* 168:501–511) has shown that uPAR, a GPI-linked 3-domain membrane receptor, associates in cis with FN matrix-engaged α5β1 through an interaction involving the BC loop of blade 4 of the integrin's β-propeller domain. Binding of the uPA/PAI-1 ligand to uPAR in the uPAR-liganded integrin complex results in detachment of the integrin from the FN matrix. Interaction of uPAR with the FN-bound α5β1 is possible in the surface-expressed bent integrin but not genu-extended form. The paper by Wei et al. (2005) thus extends our results showing that the bent integrin ectodomain stably binds FN to the native membrane-bound form of the integrin.

References

Adair, B.D., and M. Yeager. 2002. Three-dimensional model of the human platelet integrin alpha IIbbeta 3 based on electron cryomicroscopy and x-ray crystallography. *Proc. Natl. Acad. Sci. USA.* 99:14059–14064.

Arnaout, M.A. 2002. Integrin structure: new twists and turns in dynamic cell adhesion. *Immunol. Rev.* 186:125–140.

Beglova, N., S.C. Blacklow, J. Takagi, and T.A. Springer. 2002. Cysteine-rich module structure reveals a fulcrum for integrin rearrangement upon activation. *Nat. Struct. Biol.* 9:282–287.

Butta, N., E.G. Arias-Salgado, C. González-Manchón, M. Ferrer, S. Larrucea, M.S. Ayuso, and R. Parrilla. 2003. Disruption of the beta3 663-687 disulfide bridge confers constitutive activity to beta3 integrins. *Blood.* 102:2491–2497.

Cai, T.Q., S.K. Law, H.R. Zhao, and S.D. Wright. 1995. Reversible inactivation of purified leukocyte integrin CR3 (CD11b/CD18, alpha m beta 2) by removal of divalent cations from a cryptic site. *Cell Adhes. Commun.* 3:399–406.

Calzada, M.J., M.V. Alvarez, and J. González-Rodríguez. 2002. Agonist-specific structural rearrangements of integrin alpha IIbbeta 3. Confirmation of the bent conformation in platelets at rest and after activation. *J. Biol. Chem.* 277:39899–39908.

Cheresh, D.A., and R.C. Spiro. 1987. Biosynthetic and functional properties of an Arg-Gly-Asp-directed receptor involved in human melanoma cell attachment to vitronectin, fibrinogen, and von Willebrand factor. *J. Biol. Chem.* 262:17703–17711.

Chigaev, A., A.M. Blenc, J.V. Braaten, N. Kumaraswamy, C.L. Kepley, R.P. Andrews, J.M. Oliver, B.S. Edwards, E.R. Prossnitz, R.S. Larson, and L.A. Sklar. 2001. Real time analysis of the affinity regulation of alpha 4-integrin. The physiologically activated receptor is intermediate in affinity between resting and Mn^{2+} or antibody activation. *J. Biol. Chem.* 276:48670–48678.

Copié, V., Y. Tomita, S.K. Akiyama, S.-i. Aota, K.M. Yamada, R.M. Venable, R.W. Pastor, S. Krueger, and D.A. Torchia. 1998. Solution structure and dynamics of linked cell attachment modules of mouse fibronectin containing the RGD and synergy regions: comparison with the human fibronectin crystal structure. *J. Mol. Biol.* 277:663–682.

Dickinson, C.D., B. Veerapandian, X.-P. Dai, R.C. Hamlin, N.-h. Xuong, E. Ruoslahti, and K.R. Ely. 1994. Crystal structure of the tenth type III cell adhesion module of human fibronectin. *J. Mol. Biol.* 236:1079–1092.

Engel, J., E. Odermatt, A. Engel, J.A. Madri, H. Furthmayr, H. Rohde, and R. Timpl. 1981. Shapes, domain organizations and flexibility of laminin and fibronectin, two multifunctional proteins of the extracellular matrix. *J. Mol. Biol.* 150:97–120.

Erickson, H.P., and N.A. Carrell. 1983. Fibronectin in extended and compact conformations. Electron microscopy and sedimentation analysis. *J. Biol. Chem.* 258:14539–14544.

Frank, J., M. Radermacher, P. Penczek, J. Zhu, Y. Li, M. Ladjadj, and A. Leith. 1996. SPIDER and WEB: processing and visualization of images in 3D electron microscopy and related fields. *J. Struct. Biol.* 116:190–199.

Gailit, J., and E. Ruoslahti. 1988. Regulation of the fibronectin receptor affinity by divalent cations. *J. Biol. Chem.* 263:12927–12932.

Grigorieff, N. 2000. Resolution measurement in structures derived from single particles. *Acta Crystallogr. D Biol. Crystallogr.* 56:1270–1277.

Humphries, M.J. 2000. Integrin structure. *Biochem. Soc. Trans.* 28:311–339.

Hynes, R.O. 2002. Integrins: bidirectional, allosteric signaling machines. *Cell.* 110:673–687.

Kouns, W.C., D. Kirchhofer, P. Hadváry, A. Edenhofer, T. Weller, G. Pfenninger, H.R. Baumgartner, L.K. Jennings, and B. Steiner. 1992. Reversible conformational changes induced in glycoprotein IIb-IIIa by a potent and selective peptidomimetic inhibitor. *Blood.* 80:2539–2547.

Leahy, D.J., I. Aukhil, and H.P. Erickson. 1996. 2.0 Å crystal structure of a four-domain segment of human fibronectin encompassing the RGD loop and synergy region. *Cell.* 84:155–164.

Litvinov, R.I., C. Nagaswami, G. Vilaire, H. Shuman, J.S. Bennett, and J.W. Weisel. 2004. Functional and structural correlations of individual alphaIIbbeta3 molecules. *Blood.* 104:3979–3985.

Litvinovich, S.V., and K.C. Ingham. 1995. Interactions between type III domains in the 110 kDa cell-binding fragment of fibronectin. *J. Mol. Biol.* 248:611–626.

Ludtke, S.J., P.R. Baldwin, and W. Chiu. 1999. EMAN: semiautomated software for high-resolution single-particle reconstructions. *J. Struct. Biol.* 128:82–97.

Main, A.L., T.S. Harvey, M. Baron, J. Boyd, and I.D. Campbell. 1992. The three-dimensional structure of the tenth type III module of fibronectin: an insight into RGD-mediated interactions. *Cell.* 71:671–678.

Mehta, R.J., B. Diefenbach, A. Brown, E. Cullen, A. Jonczyk, D. Güssow, G.A. Luckenbach, and S.L. Goodman. 1998. Transmembrane-truncated alphavbeta3 integrin retains high affinity for ligand binding: evidence for an 'inside-out' suppressor? *Biochem. J.* 330:861–869.

Mould, A.P., E.J.H. Symonds, P.A. Buckley, J.G. Grossmann, P.A. McEwan, S.J. Barton, J.A. Askari, S.E. Craig, J. Bella, and M.J. Humphries. 2003. Structure of an integrin-ligand complex deduced from solution x-ray scattering and site-directed mutagenesis. *J. Biol. Chem.* 278:39993–39999.

Nermut, M.V., N.M. Green, P. Eason, S.S. Yamada, and K.M. Yamada. 1988. Electron microscopy and structural model of human fibronectin receptor. *EMBO J.* 7:4093–4099.

Redick, S.D., D.L. Settles, G. Briscoe, and H.P. Erickson. 2000. Defining fibronectin's cell adhesion synergy site by site-directed mutagenesis. *J. Cell Biol.* 149:521–527.

Sheehan, B., S.D. Fuller, M.E. Pique, and M. Yeager. 1996. AVS software for visualization in molecular microscopy. *J. Struct. Biol.* 116:99–106.

Takagi, J., B.M. Petre, T. Walz, and T.A. Springer. 2002. Global conformational rearrangements in integrin extracellular domains in outside-in and inside-out signaling. *Cell.* 110:599–611.

Takagi, J., K. Strokovich, T.A. Springer, and T. Walz. 2003. Structure of integrin alpha5beta1 in complex with fibronectin. *EMBO J.* 22:4607–4615.

Winzor, D.J., and H.A. Scheraga. 1963. Studies of chemically reacting systems on sephadex. I. Chromatographic demonstration of the Gilbert theory. *Biochemistry.* 172:1263–1267.

Xiao, T., J. Takagi, B.S. Coller, J.-H. Wang, and T.A. Springer. 2004. Structural basis for allostery in integrins and binding to fibrinogen-mimetic therapeutics. *Nature.* 432:59–67.

Xiong, J.-P., T. Stehle, B. Diefenbach, R. Zhang, R. Dunker, D.L. Scott, A. Joachimiak, S.L. Goodman, and M.A. Arnaout. 2001. Crystal structure of the extracellular segment of integrin alpha Vbeta3. *Science.* 294:339–345.

Xiong, J.-P., T. Stehle, R. Zhang, A. Joachimiak, M. Frech, S.L. Goodman, and M.A. Arnaout. 2002. Crystal structure of the extracellular segment of integrin alpha Vbeta3 in complex with an Arg-Gly-Asp ligand. *Science.* 296:151–155.

Xiong, J.-P., T. Stehle, S.L. Goodman, and M.A. Arnaout. 2003. New insights into the structural basis of integrin activation. *Blood.* 102:1155–1159.

Xiong, J.-P., T. Stehle, S.L. Goodman, and M.A. Arnaout. 2004. A novel adaptation of the integrin PSI domain revealed from its crystal structure. *J. Biol. Chem.* 279:40252–40254.

Zhao, F.-Q., and R. Craig. 2003. Capturing time-resolved changes in molecular structure by negative staining. *J. Struct. Biol.* 141:43–52.